Progress In Electromagnetics Research C, Vol. 124, 253–267, 2022

Research on the Built-in Tangential and Radial Combined-Pole Permanent Magnet Hub Drive Motor for Electric Vehicles

Shilong Yan[1], Xueyi Zhang[1, *], Zhidong Gao[2], Mingjun Xu[3], Lei Wang[2], Yufeng Zhang[3], Wenchao Zhang[3], and Kai Geng[3]

Abstract—In order to solve the problems of high THD (total harmonic distortion) of air-gap magnetic density, large cogging torque, and low power density of permanent magnet (PM) hub motor, a built-in tangential and radial PM combined-pole hub motor is proposed in this paper. The magnetic field provided by tangential PM is the main magnetic field, and the magnetic field provided by radial PM plays an auxiliary role in regulation, which can effectively improve the air-gap magnetic density of the motor, reduce the THD of back electromotive force (EMF), and weaken the peak value of cogging torque. Based on the equivalent magnetic circuit method, this paper analyzes the magnetic circuit of the motor, deduces the leakage magnetic flux coefficient, and reduces the leakage magnetic flux by optimizing the structure of the motor. Finally, the prototype is manufactured and tested to verify the effectiveness of finite element analysis. The results show that the designed PM hub drive motor has low THD of back EMF and good sinusoidality of waveform under no-load condition, and good output performance.

1. INTRODUCTION

With the continuous development of electric vehicle and its driving technology, due to its high transmission efficiency and high braking energy recovery rate, hub motor has become a research hotspot of driving motor for electric vehicle. Each wheel of electric vehicle driven by a hub motor is controlled independently, with reasonable power distribution, good dynamic response, and superior power performance, which is easy to realize the complex control of the vehicle, and it is considered the ultimate driving mode of electric vehicle [1–5].

For permanent magnet (PM) hub motor, researchers have carried out some studies on it. Scholars from the Université Bourgogne Franche-Comté in France proposed an axial flux built-in PM synchronous hub motor [6, 7]. The motor has two stators and a rotor, wherein the stator is made of fractional slot concentrative winding, the rotor made of soft magnetic core, and the PM is magnetized along the circumferential direction and embedded in the rotor, which improves the air-gap magnetic density and the mechanical strength of the motor. It is worth mentioning that the motor has small cogging torque, large torque, strong flux attenuation ability, and good PM performance. However, the stator and rotor of the motor are rolled from a long flat soft magnetic steel plate. The magnetic steel needs to be magnetized in sections, which is difficult to manufacture. In addition, the temperature rise of the motor is high, and the eddy current loss is large, resulting in the decline of the overall efficiency of the motor. Scholars from the Newcastle University proposed and optimized a hub motor with a built-in V-shaped PM rotor structure [8]. Each pole of the motor is jointly provided by two built-in V-shaped

Received 30 July 2022, Accepted 7 September 2022, Scheduled 29 September 2022
* Corresponding author: Xueyi Zhang (zhangxueyi@sdut.edu.cn).
[1] School of Transportation and Vehicle Engineering, Shandong University of Technology, Xincun West Road, Zhangdian District, Zibo, Shandong Province, China. [2] Weifang No. 1 Motor Factory Co., Ltd, Xiangjiang Road, Anqiu City, Shandong Province, China. [3] School of Transportation and Vehicle Engineering, Shandong University of Technology, Xincun West Road, Zhangdian District, Zibo, Shandong Province, China.

PMs, which do not face the air gap and avoid irreversible demagnetization of the PM. Compared with the traditional surface-mounted PM hub motor, the built-in V-shaped PM rotor structure has obvious magnetic gathering function, which improves the air-gap magnetic density, reduces the leakage magnetic flux, and improves the output performance of the motor. However, the high-order harmonic content of the air-gap magnetic field of the hub motor is high, and the THD (total harmonic distortion) of the air gap magnetic field waveform is also high. Scholars from Tianjin University have proposed an external rotor PM synchronous hub motor with a U-shaped rotor structure [9]. The motor adopts a U-shaped built-in PM structure to replace the traditional surface-mounted PM structure, which is conducive to improving the overall magnetic density of hub motor. Besides, the hybrid rotor structure integrates the advantages of radial rotor structure and tangential rotor structure, with relatively small leakage magnetic flux coefficient and large magnetic flux per magnetic pole. The U-shaped rotor structure has large power density, wide constant power range, large torque at low speed, and constant power at high speed. But the consumption of PM of the motor is large, and the power density of this machine is improved less than that of the motor with the same power. Scholars from the Third University of Rome, Italy, proposed a permanent disk hub drive motor [10, 11]. The motor is developed based on an axial topology structure motor. The rotor and stator are arranged in disc. The stator is sealed with epoxy resin, and the rotor is composed of two low carbon steel discs, which improves the mechanical strength and heat dissipation effect. PMs with different magnetism are placed on both sides of the rotor, and the magnetic field of the motor is distributed axially. However, the permanent disk motor has large additional air gap, long axial length, and large core loss, resulting in relatively small power density of the motor. Zhejiang Elaphe company has developed an M700 series hub motor [12–14], which adopts an external rotor and a surface-mounted structure, with the characteristics of high efficiency and low power consumption. However, the surface-mounted structure of the motor has low magnetic field strength, which cannot make full use of the reluctance torque. The matching cycle time between the motor and the traditional chassis is long, and the effect is poor, so it needs to be equipped with a special chassis module.

According to the above analysis, scholars have carried out in-depth research on the PM hub drive motor for electric vehicles and achieved some research results. However, at present, surface-mounted structure is basically used in vehicles, and the magnetic field strength of the motor is relatively small, which cannot make full use of the electromagnetic torque. In contrast, the built-in PM synchronous motor has the advantages of mature technology, compact structure, high power density, high reliability, and wide speed regulation range. It is the best choice of PM hub drive motor for electric vehicles. In spite of this, at present, built-in PM drive motor mainly has the following problems: there are many high-order harmonics in the motor air gap magnetic field, large THD of back electromotive force (EMF), and large leakage magnetic flux coefficient, so the topology structure needs to be optimized; the slotting design of the motor cannot avoid the cogging torque, so it is necessary to reduce the peak cogging torque as far as possible and improve the reliability of the motor. According to the above problems, this paper proposes a new type of rare earth PM hub motor with built-in tangential and radial combined-poles for electric vehicles. The magnetic flux of each pole of the rotor is jointly provided by adjacent radial PMs and tangential PM, which can effectively improve the air-gap magnetic density of the motor, reduce the waveform sag of the air gap magnetic field, and improve the output performance of the motor.

2. STRUCTURE AND MAGNETIC CIRCUIT MODEL OF HUB DRIVE MOTOR

2.1. Magnetic Circuit Analysis of the Motor

The built-in tangential and radial combined-pole PM hub drive motor adopts an external rotor combined-pole structure. The combined-pole is composed of tangential PM and radial PM. In order to reduce leakage magnetic flux, a fixed shape magnetic isolation air gap is designed at the end of each PM and between PMs. This magnetic pole structure has the following advantages: in the tangential and radial combined-pole structure, the tangential PM provides the main magnetic flux of the motor, and the radial permanent magnet provides only auxiliary magnetic flux, which is set to improve the concave phenomenon of the air gap magnetic field waveform and the sinusoidality of the air-gap magnetic density waveform of the motor. Compared with the surface-mounted rotor, the magnetic gathering effect of the structure is obvious, and the peak value of the air-gap magnetic density is large. The PM magnetic

pole does not directly face the air gap, which can effectively avoid the irreversible demagnetization of the PM due to the armature reaction and improve the reliability of the motor. The built-in tangential and radial combined-pole magnetic circuit has large direct axis inductance, which can make full use of reluctance torque and improve the ability of flux-weakening. The design of magnetic isolation air gap in the rotor reduces leakage magnetic flux and avoids the waste of PM materials. The overall structure of the hub motor designed in this paper is shown in Figure 1, and the main technical parameters of the hub motor are shown in Table 1.

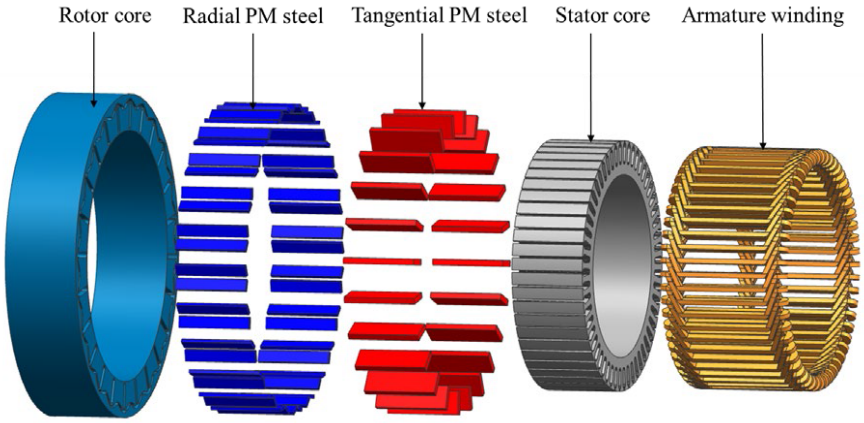

Figure 1. Structure diagram of rare earth PM hub motor with built-in tangential and radial combined-pole.

Table 1. The main technical parameters of the hub motor.

Parameter name	Value
Rated power (kW)	2
Rated torque (N·m)	31.8
Rated speed (r/min)	600
Peak power (kW)	5
Rated voltage (V)	72
Phase number	3
Rated efficiency	87.5%
Insulation grade	E

The magnetic field of the built-in tangential and radial combined-pole rotor is composed of the magnetic field provided by the radial PM and the magnetic field provided by the tangential PM. Compared with the conventional structure of pure tangential PM, the arrangement of radial PM in the combined-pole can effectively increase the magnetic flux in the center of the magnetic pole. Besides, a ship anchor type magnetic isolation air gap is set between the V-type radial PM and the tangential PM, and a wedge-type magnetic isolation air gap is set at the inner ends of the tangential PM and radial PM, which can effectively reduce the end leakage magnetic flux of the PM and avoid the waste of PM materials.

The main magnetic flux of magnetic field of each magnetic pole of the rotor is composed of main magnetic flux circuit 1 and main magnetic flux circuit 2. The magnetic potential of main magnetic flux circuit 1 is generated by tangential PM alone. The direction of magnetic circuit is tangential PM N pole → rotor core → main air gap → stator core → main air gap → rotor core → tangential PM S pole. The magnetic potential of main magnetic flux circuit 2 is generated by radial PM, and the direction of magnetic circuit is left radial PM N pole → rotor core → main air gap → stator core → main air gap →

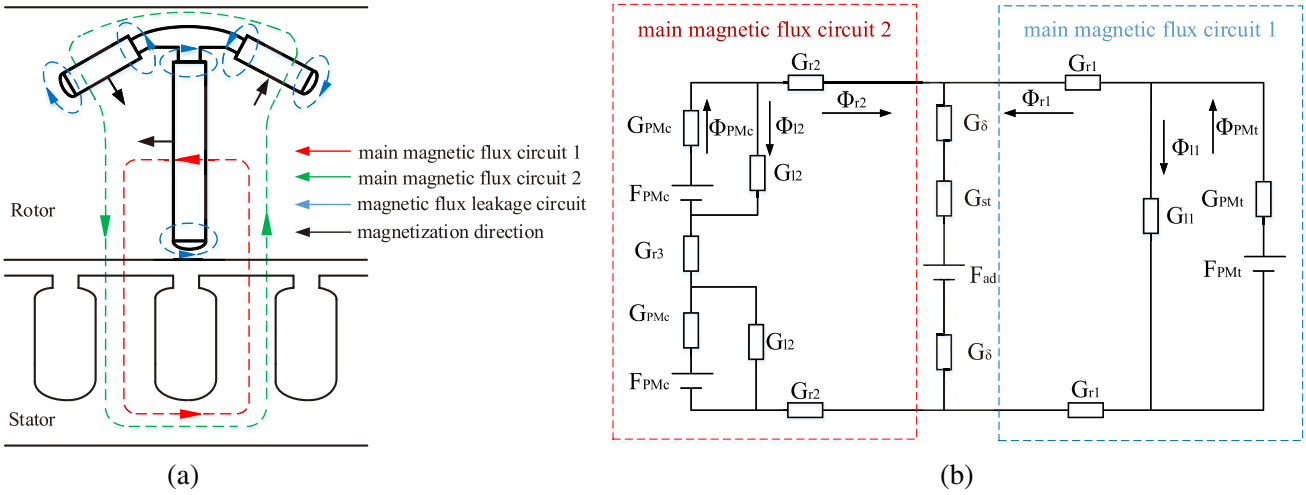

Figure 2. (a) Magnetic circuit analysis diagram. (b) The equivalent magnetic circuit model.

rotor core → right radial PM S pole → right radial PM N pole → rotor core → left radial PM S pole. The leakage magnetic flux of magnetic field of each magnetic pole of the rotor is mainly concentrated at the end of the PM. The specific distribution is shown in Figure 2(a).

According to the magnetic circuit analysis diagram of the motor, the equivalent magnetic circuit model is established, as shown in Figure 2(b). In the figure, Φ_{PMt} is the magnetic flux generated by the tangential PM in the main magnetic flux circuit 1; Φ_{PMc} is the magnetic flux generated by the radial PM in the main magnetic flux circuit 2; Φ_{r1} is the effective magnetic flux through the main air gap provided by the tangential PM in the main magnetic flux circuit 1; Φ_{r2} is the effective magnetic flux through the main air gap provided by the radial PM in the main magnetic flux circuit 2; Φ_{l1} is the leakage magnetic flux generated by the tangential PM; Φ_{l2} is the leakage magnetic flux generated by the radial PM. F_{PMt} is the magnetic potential generated by tangential PM; F_{PMc} is the magnetic potential generated by radial PM; and F_{ad} is the direct axis component of armature reaction potential. G_{PMt} and G_{PMc} are respectively the internal permeance of tangential PM and radial PM; G_{r1} is the permeance of main flux magnetic circuit 1 in the rotor core; G_{r2} and G_{r3} are the permeance of main flux magnetic circuit 2 in different parts of the rotor core; G_{l1} and G_{l2} are the leakage permeance of tangential PM and radial PM; G_δ is the permeance at the main air gap; G_{st} is the permeance at the stator core.

Among them,

$$\begin{cases} F_{PM} = H_r h_{PM} \\ G_{PM} = \dfrac{\mu_0 \mu_r L_{PM} b_{PM}}{h_{PM}} \\ G_r = \dfrac{\mu_r A_r}{l_r} \\ G_\delta = \dfrac{\pi \mu_0 D_{id} L_s}{2p\delta} \\ G_{st} = \dfrac{\mu_r b_t L_s}{h_s} + \dfrac{Z \mu_r h_y L_s}{\pi k_{st} \left(D_{id} + h_y\right)} \end{cases} \tag{1}$$

where H_r is the coercivity of the PM; h_{PM} is the length in the magnetization direction of the PM; μ_0 is the vacuum permeability; μ_r is the permeability of the PM; L_{PM} is the axial length of the PM; b_{PM} is the thickness of the PM; A_r is the cross-sectional area of the magnetic flux generated by the PM in the rotor; l_r is the length of the magnetic circuit in the rotor core; D_{id} is the inner diameter of the stator; L_s is the axial length of the stator; p is the number of pole pairs; δ is the length of the main air gap of the motor; b_t is the width of the stator teeth; h_s is the height of the stator teeth; h_y is the height of the stator yoke; and k_{st} is the number of stator teeth through which the magnetic flux in the stator passes.

Based on the equivalent magnetic circuit model and according to Kirchhoff's law of magnetic circuit, the main magnetic flux magnetic circuit 1 can be analyzed as follows:

$$\begin{cases} \Phi_{PM1} = \Phi_{r1} + \Phi_{l1} \\ F_{PMt} = \Phi_{PM1} \cdot \dfrac{1}{G_{PMt}} + \Phi_{l1} \cdot \dfrac{1}{G_{l1}} \\ \Phi_{l1} \cdot \dfrac{1}{G_{l1}} = \Phi_{r1} \left(\dfrac{2}{G_{r1}} + \dfrac{2}{G_{\delta}} + \dfrac{1}{G_{st}} \right) + F_{ad} \end{cases} \tag{2}$$

For equation group (2), the solution can be obtained:

$$\begin{cases} \Phi_{PM1} = \dfrac{\begin{array}{c} F_{PMt}G_{\delta}G_{l1}G_{PMt}G_{r1} - F_{ad}G_{\delta}G_{PMt}G_{r1}G_{st} + 2F_{PMt}G_{\delta}G_{l1}G_{PMt}G_{st} \\ +F_{PMt}G_{\delta}G_{PMt}G_{r1}G_{st} + 2F_{PMt}G_{l1}G_{PMt}G_{r1}G_{st} \end{array}}{\begin{array}{c} G_{\delta}G_{l1}G_{r1} + 2G_{\delta}G_{l1}G_{st} + G_{\delta}G_{PMt}G_{r1} + 2G_{\delta}G_{PMt}G_{st} \\ +G_{\delta}G_{r1}G_{st} + 2G_{l1}G_{r1}G_{st} + 2G_{PMt}G_{r1}G_{st} \end{array}} \\ \Phi_{r1} = \dfrac{\begin{array}{c} -F_{ad}G_{\delta}G_{l1}G_{r1}G_{st} - F_{ad}G_{\delta}G_{PMt}G_{r1}G_{st} + F_{PMt}G_{\delta}G_{PMt}G_{r1}G_{st} \end{array}}{\begin{array}{c} G_{\delta}G_{l1}G_{r1} + 2G_{\delta}G_{l1}G_{st} + G_{\delta}G_{PMt}G_{r1} + 2G_{\delta}G_{PMt}G_{st} \\ +G_{\delta}G_{r1}G_{st} + 2G_{l1}G_{r1}G_{st} + 2G_{PMt}G_{r1}G_{st} \end{array}} \\ \Phi_{l1} = \dfrac{G_{l1}\left(\begin{array}{c} F_{ad}G_{\delta}G_{r1}G_{st} + F_{PMt}G_{\delta}G_{PMt}G_{r1} \\ +2F_{PMt}G_{\delta}G_{PMt}G_{st} + 2F_{PMt}G_{PMt}G_{r1}G_{st} \end{array} \right)}{\begin{array}{c} G_{\delta}G_{l1}G_{r1} + 2G_{\delta}G_{l1}G_{st} + G_{\delta}G_{PMt}G_{r1} + 2G_{\delta}G_{PMt}G_{st} \\ +G_{\delta}G_{r1}G_{st} + 2G_{l1}G_{r1}G_{st} + 2G_{PMt}G_{r1}G_{st} \end{array}} \end{cases} \tag{3}$$

Similarly, according to Kirchhoff's law of magnetic circuit, the analysis of main magnetic flux circuit 2 can be obtained:

$$\begin{cases} \Phi_{PMc} = \Phi_{r2} + \Phi_{l2} \\ F_{PMc} = \Phi_{PMc}\dfrac{1}{G_{PMc}} + \Phi_{l2}\dfrac{1}{G_{l2}} \\ 2\Phi_{l2}\dfrac{1}{G_{l2}} = \Phi_{r2}\left(\dfrac{2}{G_{r2}} + \dfrac{2}{G_{\delta 2}} + \dfrac{1}{G_{st}} + \dfrac{1}{G_{r3}} \right) + F_{ad} \end{cases} \tag{4}$$

For equation group (4), the solution can be obtained:

$$\begin{cases} \Phi_{PM2} = \dfrac{\begin{array}{c} F_{PMc}G_{d2}G_{l2}G_{PMc}G_{r2}G_{r3} - F_{ad}G_{d2}G_{PMc}G_{r2}G_{r3}G_{st} + F_{PMc}G_{d2}G_{l2}G_{PMc}G_{r2}G_{st} \\ +2F_{PMc}G_{d2}G_{l2}G_{PMc}G_{r3}G_{st} + 2F_{PMc}G_{d2}G_{PMc}G_{r2}G_{r3}G_{st} + 2F_{PMc}G_{l2}G_{PMc}G_{r2}G_{r3}G_{st} \end{array}}{\begin{array}{c} G_{d2}G_{l2}G_{r2}G_{r3} + G_{d2}G_{l2}G_{r2}G_{st} + 2G_{d2}G_{l2}G_{r3}G_{st} + G_{d2}G_{PMc}G_{r2}G_{r3} + G_{d2}G_{PMc}G_{r2}G_{st} \\ +2G_{d2}G_{PMc}G_{r3}G_{st} + 2G_{d2}G_{r2}G_{r3}G_{st} + 2G_{l2}G_{r2}G_{r3}G_{st} + 2G_{PMc}G_{r2}G_{r3}G_{st} \end{array}} \\ \Phi_{r2} = \dfrac{\begin{array}{c} 2F_{PMc}G_{d2}G_{PMc}G_{r2}G_{r3}G_{st} - F_{ad}G_{d2}G_{l2}G_{r2}G_{r3}G_{st} - F_{ad}G_{d2}G_{PMc}G_{r2}G_{r3}G_{st} \end{array}}{\begin{array}{c} G_{d2}G_{l2}G_{r2}G_{r3} + G_{d2}G_{l2}G_{r2}G_{st} + 2G_{d2}G_{l2}G_{r3}G_{st} + G_{d2}G_{PMc}G_{r2}G_{r3} + G_{d2}G_{PMc}G_{r2}G_{st} \\ +2G_{d2}G_{PMc}G_{r3}G_{st} + 2G_{d2}G_{r2}G_{r3}G_{st} + 2G_{l2}G_{r2}G_{r3}G_{st} + 2G_{PMc}G_{r2}G_{r3}G_{st} \end{array}} \\ \Phi_{l2} = \dfrac{G_{l2}\left(\begin{array}{c} F_{ad}G_{d2}G_{r2}G_{r3}G_{st} + F_{PMc}G_{d2}G_{PMc}G_{r2}G_{r3} + F_{PMc}G_{d2}G_{PMc}G_{r2}G_{st} \\ +2F_{PMc}G_{d2}G_{PMc}G_{r3}G_{st} + 2F_{PMc}G_{PMc}G_{r2}G_{r3}G_{st} \end{array} \right)}{\begin{array}{c} G_{d2}G_{l2}G_{r2}G_{r3} + G_{d2}G_{l2}G_{r2}G_{st} + 2G_{d2}G_{l2}G_{r3}G_{st} + G_{d2}G_{PMc}G_{r2}G_{r3} + G_{d2}G_{PMc}G_{r2}G_{st} \\ +2G_{d2}G_{PMc}G_{r3}G_{st} + 2G_{d2}G_{r2}G_{r3}G_{st} + 2G_{l2}G_{r2}G_{r3}G_{st} + 2G_{PMc}G_{r2}G_{r3}G_{st} \end{array}} \end{cases} \tag{5}$$

The leakage magnetic flux coefficient of PM hub drive motor can be calculated as:

$$\sigma = \frac{\Phi_{PM1} + \Phi_{PM2}}{\Phi_{r1} + \Phi_{r2}} \tag{6}$$

The auxiliary surface was established in the finite element software to measure the main magnetic flux and leakage magnetic flux, and the comparison between the finite element analysis results and calculation results of the equivalent magnetic circuit method is shown in Table 2.

Table 2. Comparison table between equivalent magnetic circuit method and finite element method.

Parameter name	Equivalent magnetic circuit method	Finite element method
Main flux of each pole of PM magnetic field/Wb	1.97×10^{-3}	1.92×10^{-3}
Main air gap flux of each pole of PM magnetic field/Wb	1.61×10^{-3}	1.51×10^{-3}
Leakage flux at the end of the radial PM/Wb	5.85×10^{-5}	5.32×10^{-5}
Leakage flux at the end of the tangential PM/Wb	3.60×10^{-4}	3.41×10^{-4}
No-load leakage magnetic flux coefficient	1.22	1.27

It can be seen from Table 2 that the finite element analysis results are basically consistent with the calculation results, which verifies the correctness of the equivalent magnetic circuit model. The built-in tangential and radial combined-pole rotor structure provides the magnetic flux of each pole jointly by radial PM and tangential PM. The built-in arrangement of tangential PM can effectively improve the magnetic field strength and avoid the irreversible demagnetization of PM caused by armature reaction. However, the built-in arrangement of PM has relatively large leakage magnetic flux coefficient, which will reduce the utilization rate of PM materials. Therefore, effective measures must be taken to reduce the occurrence of leakage magnetic flux and improve the power density and overall performance of the motor. Through the derivation of leakage magnetic flux coefficient, it can be seen that setting effective magnetic isolation air gap, optimizing the size of PM, and optimizing the size of stator slot can reduce leakage magnetic flux and improve the electromagnetic performance of the motor. Therefore, the following section will mainly study the influence of the above methods on the electromagnetic performance of the motor.

2.2. Analysis of the Cogging Torque of the Motor

The cogging torque T_{cog} of PM motor is defined as the negative derivative of the magnetic field energy W of the motor to the relative position angle α between the stator and the rotor when the motor is not energized, and the magnetic field energy stored in the motor is approximately equal to the sum of the magnetic field energy of the air gap and the magnetic field energy of the PM, so the cogging torque can be expressed as follows:

$$T_{cog} = -\frac{\partial W}{\partial \alpha} = -\frac{\partial (W_{PM} + W_{air})}{\partial \alpha} = -\frac{\partial \left(\dfrac{1}{2\mu_0} \displaystyle\int_V B^2(\theta, \alpha) dV \right)}{\partial \alpha} \tag{7}$$

where W_{PM} is the magnetic field energy of the PM; W_{air} is the magnetic field energy of air gap; μ_0 is the vacuum permeability; $B(\theta, \alpha)$ is the distribution function of the air-gap magnetic density along the circumference, ignoring the magnetic pressure drop of ferromagnetic materials, $B(\theta, \alpha) = B_r(\theta) G(\theta, \alpha)$, where $B_r(\theta)$ is the distribution function of the PM remanence along the circumference; $G(\theta, \alpha)$ is the distribution function of the effective air gap relative permeance along the circumference; θ is the rotor position angle; $\theta = 0$ is on the center line of the PM.

Carry out Fourier expansion on 1 and 2 and bring them into Equation (7) to obtain:

$$T_{cog}(\alpha) = \frac{\pi Z L_a}{4\mu_0} \left(R_2^2 - R_1^2 \right) \sum_{n=1}^{\infty} n G_n B_{rn} \sin(nZ\alpha) \tag{8}$$

where Z is the number of stator slots; L_a is the axial length of the stator core; R_2 is the inner circle radius of the stator; R_1 is the outer circle radius of the rotor; G_n is the n-th Fourier expansion coefficient

of the square of the relative permeability of the air gap; B_{rn} is the Fourier decomposition coefficient of the square of the air-gap magnetic density.

As can be seen from Equation (8), the cogging torque is affected by specific air-gap magnetic density harmonics. Therefore, the size of PM and stator slot parameters can be optimized to change the air-gap magnetic density distribution function and reduce its harmonic content to weaken the cogging torque.

3. PERFORMANCE OPTIMIZATION OF THE MOTOR

3.1. Influence of Magnetic Isolation Air Gap on Electromagnetic Performance

The rotor of the motor is made of silicon steel sheet DW310-35 by lamination, and its magnetic conductivity is thousands of times that of air. Therefore, on the basis of ensuring the mechanical strength of the rotor, designing a reasonable magnetic isolation air gap can effectively reduce leakage magnetic flux and avoid the waste of PM materials. The shape of the traditional magnetic isolation air gap is shown in Figure 3(a), and the new ship anchor magnetic isolation air gap designed for the built-in radial and tangential combined-pole PM hub drive motor is shown in Figure 3(b).

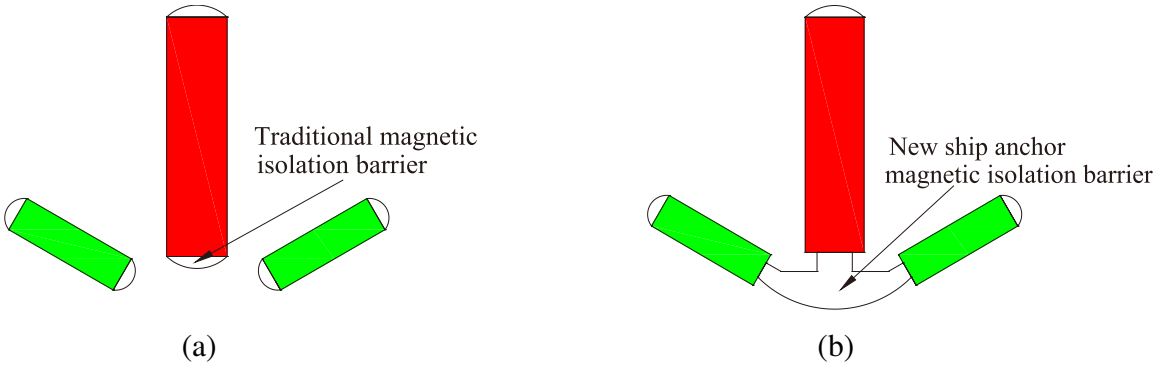

Figure 3. Different shapes of Magnetic isolation air gaps: (a) Traditional magnetic isolation air gap. (b) New ship anchor magnetic isolation air gap.

Under the condition that other parameters are the same, the finite element model of the motor with different shapes of magnetic isolation air gap is simulated. The distribution diagram of the magnetic field line and the air-gap magnetic density curve are shown in Figure 4 and Figure 5(a), and the comparison diagram of harmonic amplitude of air-gap magnetic density is shown in Figure 5(b).

It can be seen from Figure 4 that the magnetic field lines of tangential PM and radial PM of the motor with traditional magnetic isolation air gap form a closed loop at their respective ends. The magnetic leakage phenomenon is very serious, and the magnetic field provided by radial PM for the main air gap is very limited, resulting in the waste of PM. In contrast, the leakage magnetic flux paths of tangential PM and radial PM of the motor with ship anchor magnetic isolation air gap increase, and the leakage magnetic flux decreases. There is only a small part of leakage magnetic flux at the minimum connection, which is inevitable on the premise of ensuring the mechanical strength of the rotor.

It can be seen from Figure 5(a) that the waveforms of air-gap magnetic density curve of the motor with traditional magnetic isolation air gap and that of the motor with ship anchor magnetic isolation air gap are basically the same, but the amplitude of air-gap magnetic density curve of the motor with ship anchor magnetic isolation air gap is higher. As can be seen from Figure 5(b), the amplitude of fundamental wave of air-gap magnetic density of the motor with the new-type anchor-type magnetic isolation air gap increases significantly, and the amplitude of other harmonics also changes, but the variation is not significant. Therefore, the use of new ship anchor type magnetic isolation air gap can effectively reduce leakage magnetic flux, increase the air-gap magnetic density of the motor, and improve the utilization rate of PM materials.

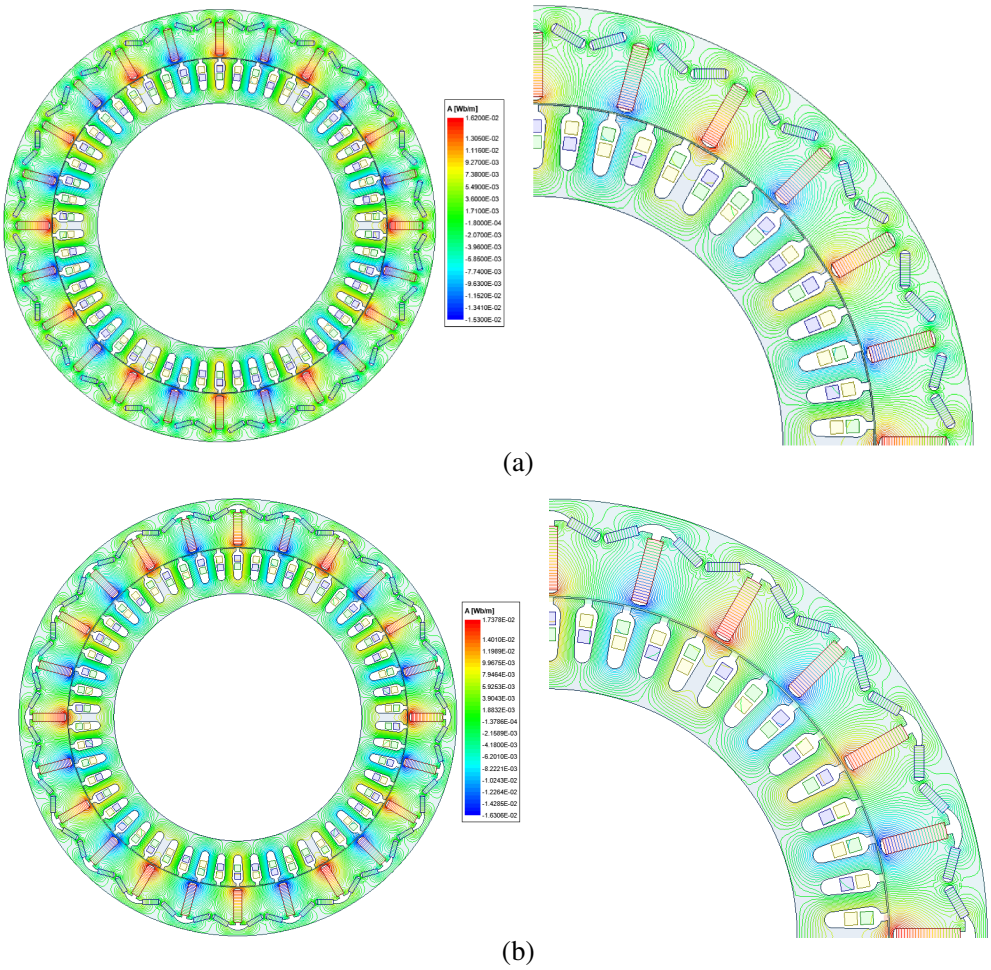

Figure 4. Distribution diagram of magnetic field line under different magnetic isolation air gaps. (a) Distribution diagram of magnetic field line with traditional magnetic isolation air gap. (b) Distribution diagram of the magnetic field line with new ship anchor type magnetic isolation air gap.

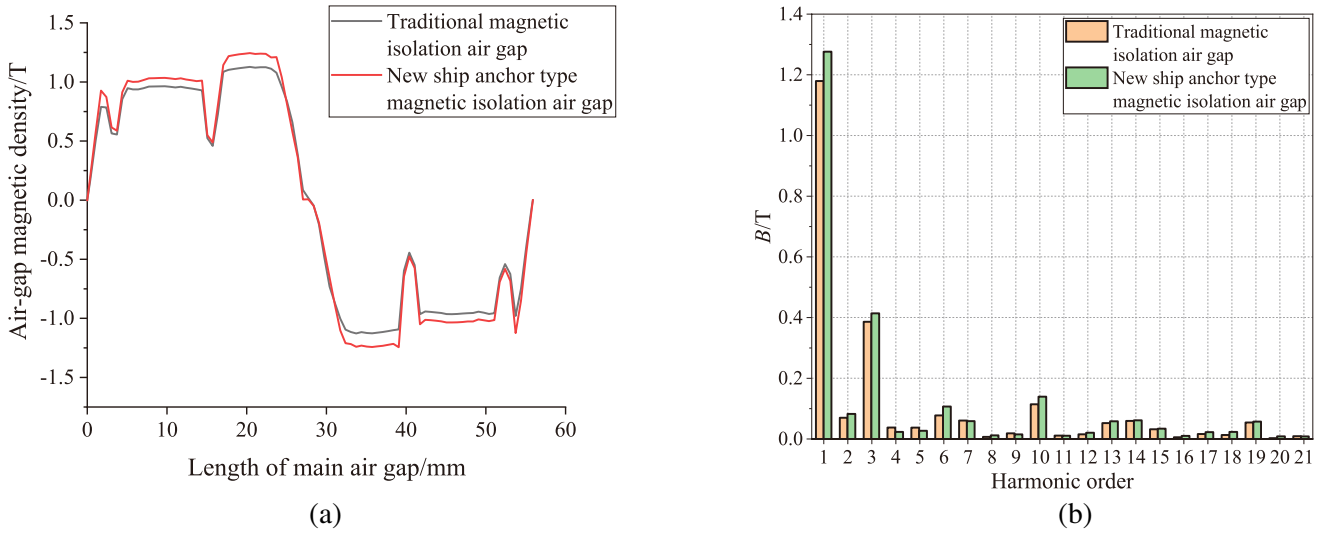

Figure 5. (a) Comparison diagram of air-gap magnetic density curve. (b) Comparison diagram of harmonic amplitude of air-gap magnetic density.

3.2. Effect of Size of PM on Electromagnetic Performance

From the previous derivation, the size of PM will affect the leakage magnetic flux coefficient of the motor. In order to study the influence law of the size of PM on the electromagnetic performance of the motor, it is parameterized. The length of tangential PM in the magnetization direction and width of PM are defined as h_{m1} and b_{m1}, and the length of radial PM in the magnetization direction and width of PM are h_{m2} and b_{m2}. It is optimized and analyzed by finite element method.

Set the initial value of the length h_{m1} in the magnetization direction of tangential PM as 5 mm and the width b_{m1} as 20 mm, and the length h_{m2} in the magnetization direction of radial PM as 3 mm and the width b_{m2} as 10 mm. When h_{m1} is $4 \sim 6$ mm, the step size is 0.5 mm; b_{m1} is $18 \sim 22$ mm; the step size is 1 mm; h_{m2} is $2 \sim 4$ mm; the step size is 0.5 mm; b_{m2} is $9 \sim 11$ mm; the step size is 0.5 mm. The peak value of air-gap magnetic density curve, peak value of cogging torque, and variation curve of the THD of back EMF obtained by simulation are shown in Figure 6 and Figure 7 respectively.

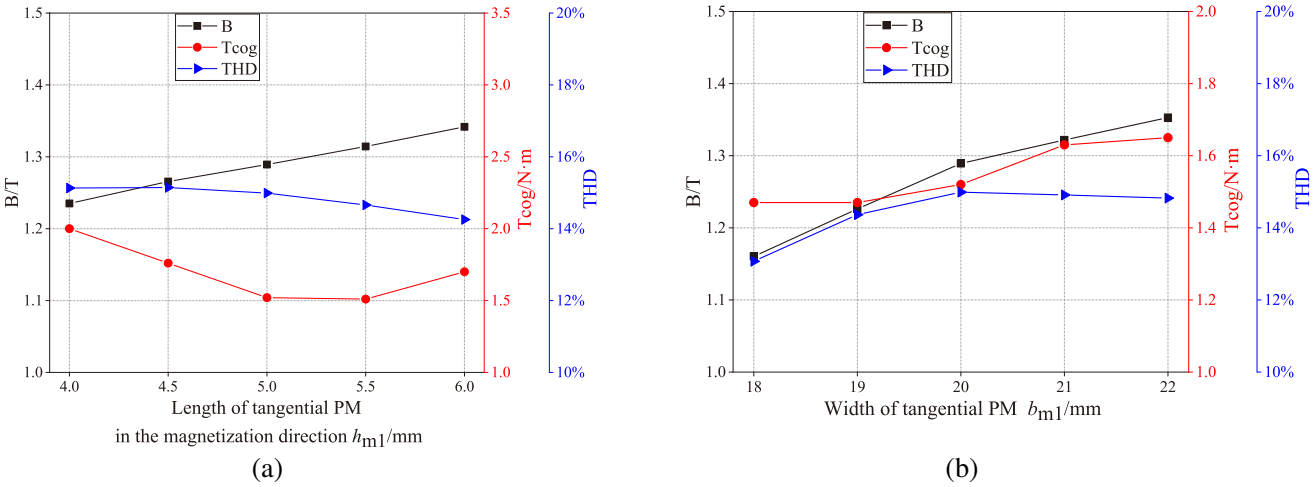

Figure 6. Influence of size parameters of tangential PM on electromagnetic performance.

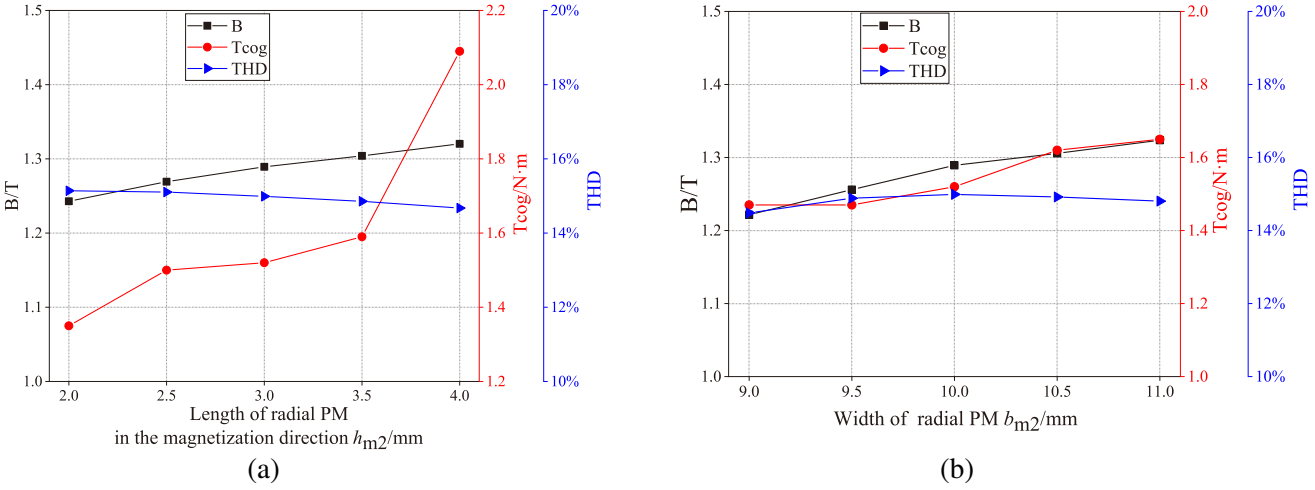

Figure 7. Influence of size parameters of radial PM on electromagnetic performance.

It can be seen from the figure that the amplitude of fundamental wave of air-gap magnetic density shows an increasing trend with the increase of PM size parameters. Compared with radial PM steel, the change of tangential PM size parameters has a more obvious effect on air-gap magnetic density. Similarly, the change of size parameters of tangential PM has a great impact on the THD of back EMF

of the motor. The THD of back EMF increases with the increase of the length of tangential PM in the magnetization direction, and first increases and then tends to ease with the increase of its width. This is consistent with the design of the motor structure. The tangential PM provides the main magnetic flux, and the magnetic field generated by the radial PM plays an auxiliary role. Therefore, the change of tangential PM parameters has an obvious impact on the magnetic field characteristics and output characteristics of the motor. In addition, it can be seen from the figure that the length of tangential PM in the magnetization direction has a great influence on the cogging torque, and the peak value of cogging torque fluctuates greatly with the increase of its length. In contrast, the influence of other PM size parameters on cogging torque is not obvious, and the fluctuation is within 0.1 N·m. Considering the air-gap magnetic density, cogging torque, and the THD of back EMF of the motor, the optimized size parameters of PM are $h_{m1} = 5$ mm, $b_{m1} = 20$ mm, $h_{m2} = 3$ mm, and $b_{m2} = 10$ mm.

3.3. Influence of Stator Slot Size on Electromagnetic Performance

By deducing the magnetic flux leakage coefficient, it can be seen that the width of stator tooth and height of stator tooth will affect the magnetic flux leakage coefficient, so the size of stator slot can be optimized to reduce the magnetic flux leakage effect of the motor. The schematic diagram of various parameters of stator slot is shown in Figure 8.

In Figure 8, b_{s0} is the width of the stator slot notch; b_{s1} is the width of stator slot upper bottom; b_{s2} is the width of stator slot lower bottom; h_{s0} is the height of stator slot notch; h_{s2} is the depth of stator slot.

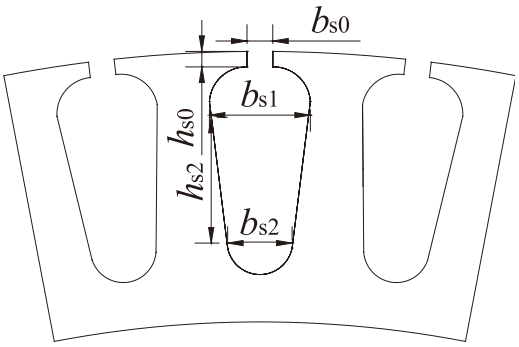

Figure 8. Influence of size parameters of radial PM on electromagnetic performance.

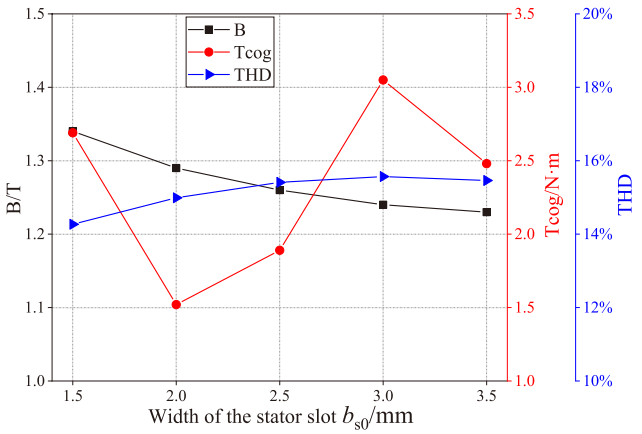

Figure 9. Influence of the width of the stator slot b_{s0} on electromagnetic performance.

The initial parameters of stator slot of built-in tangential and radial PM hub drive motor are: $b_{s0} = 2.0$ mm, $h_{s0} = 2.0$ mm, $b_{s1} = 8.0$ mm, $b_{s2} = 5.0$ mm, $h_{s2} = 12.0$ mm.

The value range of the width of the stator slot notch b_{s0} is $1.5 \sim 3.5$ mm, and the step size is 0.5 mm. The variation curves of the amplitude of fundamental wave of air-gap magnetic density, cogging torque peak, and the THD of back EMF under different stator slot widths are obtained by simulation, as shown in Figure 9.

Figure 9 shows that with the increase of the width of the stator slot notch b_{s0}, the amplitude of fundamental wave of air-gap magnetic density of the motor decreases, and the decreasing trend is more and more gentle, while the THD of the back EMF of the motor increases, and the increasing trend slows down after $b_{s0} = 2.5$ mm. In contrast, the peak value of motor cogging torque fluctuates obviously with b_{s0}, and the peak value is the smallest when $b_{s0} = 2$ mm. Considering comprehensively, $b_{s0} = 2$ mm is determined as the best parameter value.

The width of stator slot upper bottom b_{s1} ranges from 7.0 to 9.0 mm in steps of 0.5 mm, and the width of stator slot lower bottom b_{s2} ranges from 4.0 to 6.0 mm in steps of 0.5 mm. The variation curves of the amplitude of fundamental wave of air-gap magnetic density, peak value of cogging torque, and

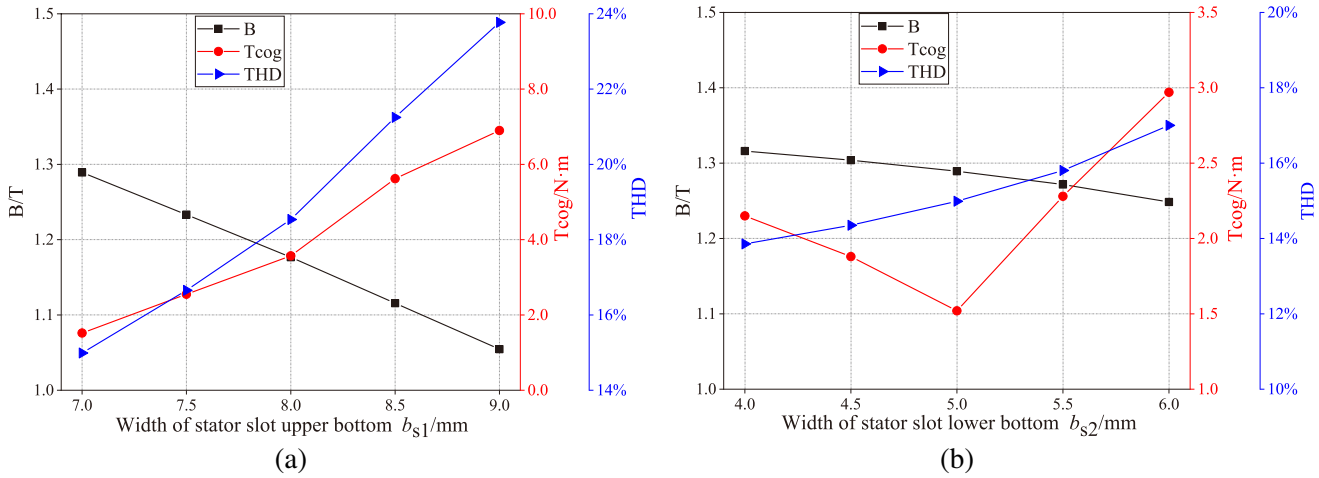

Figure 10. (a) Influence of width of stator slot upper bottom b_{s1} on electromagnetic performance. (b) Influence of width of stator slot lower bottom b_{s2} on electromagnetic performance.

the THD of back EMF under different parameters are obtained by simulation, as shown in Figure 10(a) and Figure 10(b).

It can be seen from Figure 10(a) that with the increase of b_{s1}, the amplitude of fundamental wave of air-gap magnetic density of the motor decreases. When $b_{s1} = 7$ mm, the amplitude of fundamental wave of air-gap magnetic density reaches the maximum value. The THD of back EMF increases with the increase of b_{s1}. When $b_{s1} = 7$ mm, the THD is the smallest. Similarly, the peak value of cogging torque increases with the increase of b_{s1}. Figure 10(b) shows that when b_{s2} changes, the variation trend of the amplitude of fundamental wave of air-gap magnetic density and the THD of back EMF is the same as that of b_{s1}; however, by comparison, the influence of b_{s2} on it is obviously smaller, and the variation amplitude of the curve is also smaller. The peak value of cogging torque increases first and then decreases, when $b_{s2} = 5$ mm, and the peak value of cogging torque is the smallest.

Since the upper bottom width of the stator slot should match with the lower bottom width of the stator slot, the two parameters are jointly simulated to obtain the amplitude of fundamental wave of air-gap magnetic density, cogging torque peak, and the THD of back EMF under different parameter matching, as shown in Figure 11.

Figure 11 shows that the width of the stator slot upper bottom has a great influence on the amplitude of fundamental wave of air-gap magnetic density, and a smaller width of the stator slot

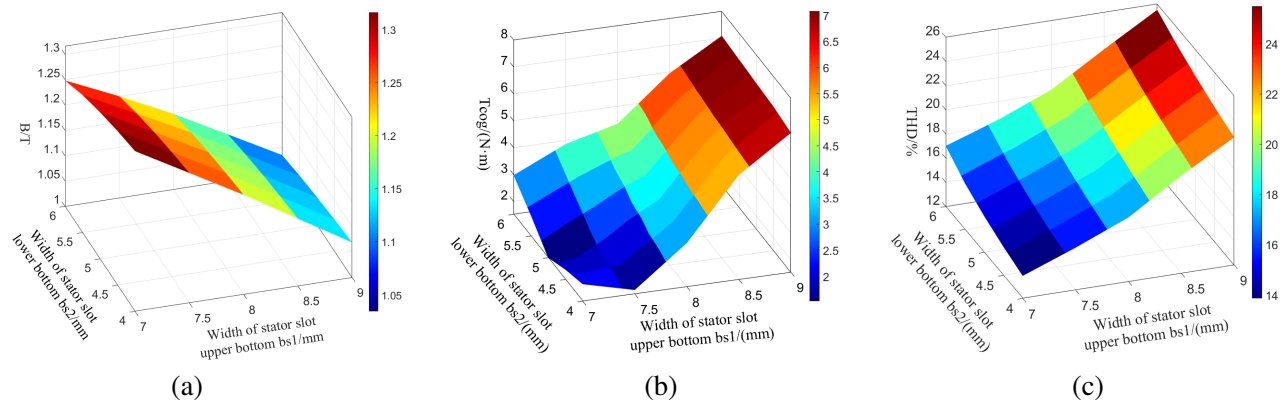

Figure 11. Electromagnetic performance variation diagrams under different width of stator slot matching.

upper bottom can obtain a larger air-gap magnetic density. Similarly, compared with the width of the stator slot lower bottom, the influence of the width of the stator slot upper bottom on the cogging torque is more obvious. With the increase of the width of the stator slot upper bottom, the peak value of the cogging torque increases significantly. It can be seen from the figure that the combination of smaller width of stator slot upper bottom and smaller width of stator slot lower bottom can effectively reduce the cogging torque. Similar to the variation surface of the peak value of cogging torque, the THD of back EMF also increases significantly with the increase of the width of stator slot upper bottom and the width of stator slot lower bottom. Therefore, through comprehensive analysis, $b_{s1} = 7\,\text{mm}$ and$b_{s2} = 5\,\text{mm}$ are selected as the best parameter values.

The value range of the height of stator slot notch h_{s0} is $0.5 \sim 2.5\,\text{mm}$, and the step size is 0.5 mm. The value range of the depth of stator slot h_{s2} is $10.0 \sim 14.0\,\text{mm}$, and the step size is 0.5 mm. The variation curves of the amplitude of fundamental wave of air-gap magnetic density, cogging torque peak, and the THD of back EMF under different parameters are shown in Figure 12(a) and Figure 12(b).

Figure 12(a) shows that with the increase of the height of stator slot notch h_{s0}, the amplitude of fundamental wave of air-gap magnetic density increases slightly, but the change is not obvious. The peak curve of cogging torque fluctuates greatly, and when $h_{s0} = 2\,\text{mm}$, the minimum value is obtained.

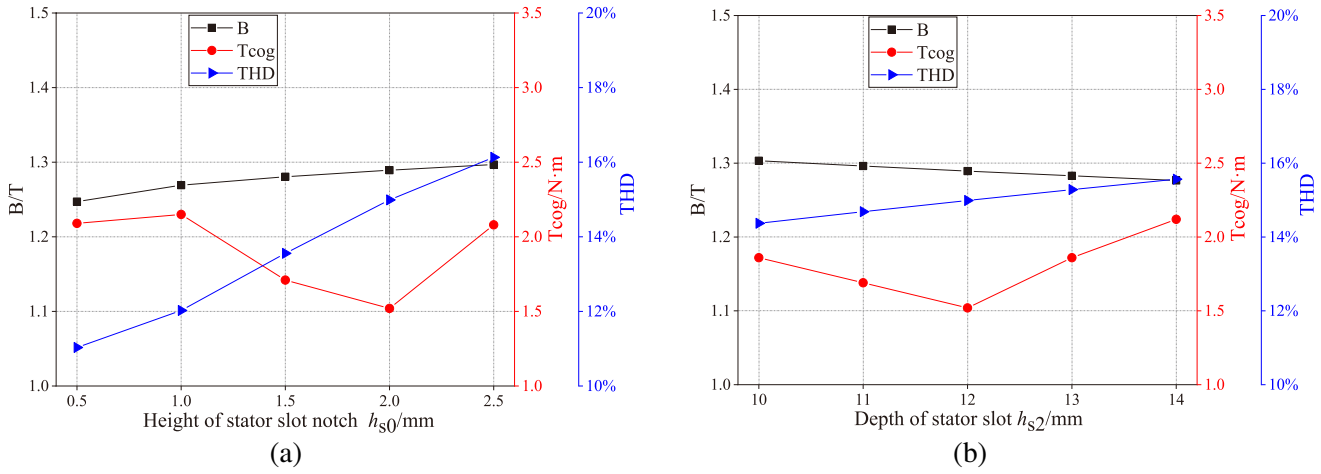

Figure 12. (a) Influence of the height of stator slot notch h_{s0} on electromagnetic performance. (b) Influence of the depth of stator slot h_{s2} on electromagnetic performance.

Table 3. Optimized parameters of the motor.

Parameter name	Parameter value
Length of tangential PM in magnetization direction h_{m1}/mm	5
Width of tangential PM b_{m1}/mm	20
Length of radial PM in magnetization direction h_{m2}/mm	3
Width of radial PM b_{m2}/mm	10
Width of stator slot notch b_{s0}/mm	2
Height of stator slot notch h_{s0}/mm	2
Width of stator slot upper bottomb_{s1}/mm	7
Width of stator slot lower bottom b_{s2}/mm	5
Depth of stator slot h_{s2}/mm	12

The THD of back EMF shows an obvious increasing trend. Through comprehensive analysis, 2 mm is selected as the best parameter value for the height of stator slot.

Figure 12(b) shows that with the increase of the depth of stator slot h_{s2}, the amplitude of fundamental wave of air-gap magnetic density gradually decreases, and the THD of back EMF gradually increases, but the amplitude of both changes is limited, while the peak value of cogging torque first decreases and then increases, and the minimum value is obtained at 12 mm. Considering that h_{s2} has no obvious effect on the amplitude of fundamental wave of air-gap magnetic density and the THD of back EMF, the depth of stator slot corresponding to the smallest peak value of cogging torque, namely $h_{s2} = 12$ mm, is selected as the best parameter value.

To sum up, the selection of parameters of PM and stator slot after optimization is shown in Table 3.

4. COMPARATIVE ANALYSIS AND VERIFICATION

According to the optimized parameters, the prototype is trial-produced and tested. The rotor structure diagram and test bench are shown in Figure 13.

The experiment is carried out on the hub drive motor under no-load condition, and the comparison

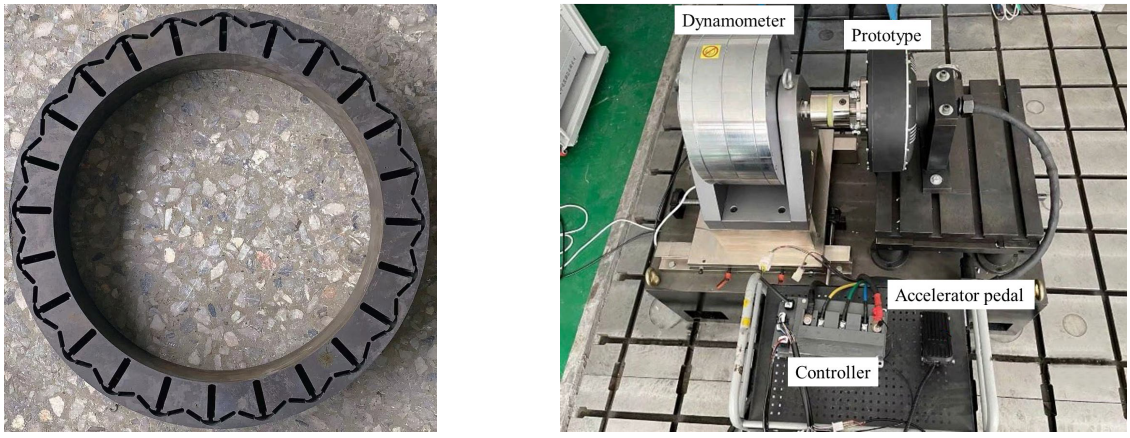

Figure 13. Photos of prototype rotor and test bench: (a) The prototype rotor. (b) The test bench.

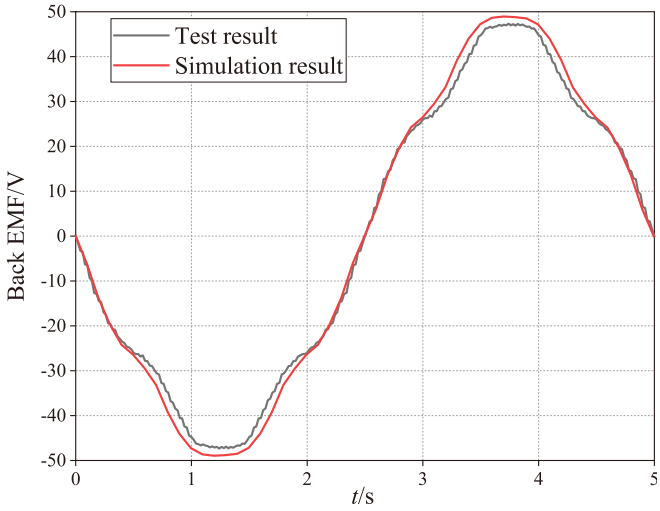

Figure 14. Comparison of test results and simulation results of back EMF.

diagram between the output back EMF curve of the motor under no-load condition and the back EMF curve obtained by simulation is shown in Figure 14.

It can be seen from Figure 14 that the back EMF curve obtained from the experiment is basically consistent with the simulation results; the peak value is lower than the finite element simulation results; and the curve depression near the peak value is large. In general, the waveform is basically sinusoidal, and the output performance is good.

The efficiency map of the motor is shown in Figure 15.

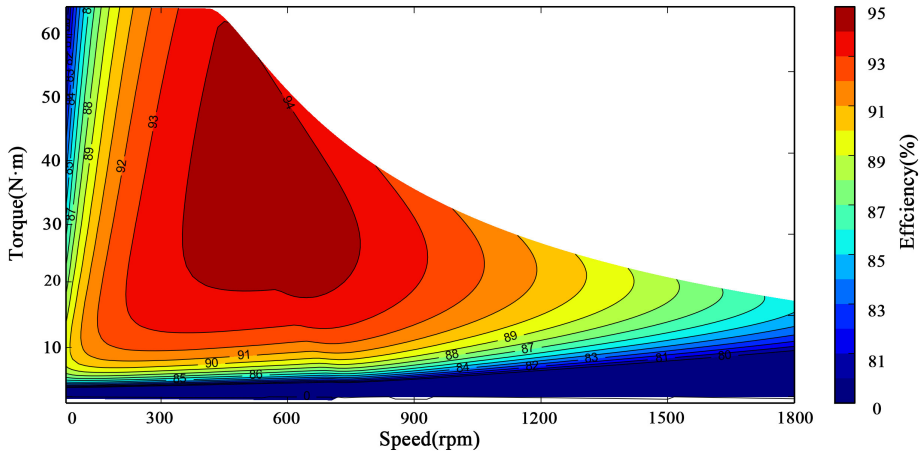

Figure 15. Efficiency map of the motor.

It can be seen from Figure 15 that the peak torque of the motor can reach 63.8 N·m, and the maximum efficiency can reach 95%. The maximum efficiency is distributed near the rated point. With the increase of the speed, the efficiency of the hub motor decreases. The speed corresponding to the peak torque inflection point is slightly lower than the rated speed, and the output performance of the motor is better.

5. CONCLUSION

This paper proposes a rare earth PM hub drive motor with built-in tangential and radial combined-pole. The motor adopts a tangential and radial combined-pole structure. The tangential PM provides the main magnetic flux, and the radial PM plays an auxiliary role, which improves the concave phenomenon of air gap magnetic field waveform, enhances the sinusoidality of air-gap magnetic density waveform of the motor, and has the advantages of high power density and good output performance. In this paper, the equivalent magnetic circuit model of the motor is established, and the no-load leakage magnetic flux coefficient of the motor is derived and calculated. Besides, magnetic isolation air gap, the size of PM, and stator slot parameters are optimized aiming at the amplitude of fundamental wave of air-gap magnetic density, cogging torque, and the THD of back EMF. After the optimization, the amplitude of fundamental wave of air-gap magnetic density of the motor is increased by 8.5%; the cogging torque of the motor is reduced by 31.8%; and the THD of back EMF is reduced by 12.5%. Finally, according to the optimized parameters, the prototype is manufactured and tested. The back EMF curve obtained by the test is basically consistent with the simulation results, which verifies the correctness of the finite element analysis. The maximum efficiency of the motor can reach 95%, indicating that the hub motor has good output performance.

ACKNOWLEDGMENT

This research was funded by the National Natural Science Foundation of China, grant number (51875327) and the Major Scientific and Technological Innovation Projects (2019JZZY020112).

REFERENCES

1. Huang, Q. R., L. Zheng, Y. N. Li, et al., "A study on the in-wheel motor control strategy for four-wheel independent drive electric vehicles," *Automotive Engineering*, Vol. 36, No. 10, 1237–1242, 2014.
2. Yu, Z. P., Y. Feng, and L. Xiong, "Review on vehicle dynamics control of distributed drive electric vehicle," *Journal of Mechanical Engineering*, Vol. 49, No. 8, 105–114, 2013.
3. Wang, R., Y. Chen, D. Feng, et al., "Development and performance characterization of an electric ground vehicle with independently actuated in-wheel motors," *Journal of Power Sources*, Vol. 196, No. 8, 3962–3971, 2011.
4. Li, G. and C. F. Zong, "Review on electric vehicle with four-wheel independent drive in-wheel motors," *Journal of Liaoning University of Technology (Natural Science Edition)*, Vol. 34, No. 1, 47–52, 2014.
5. Kamiya, K., J. Okuse, K. Ooishi, et al., "Development of in-wheel motor system for micro EV," *Proceedings of the 18th International Electric Vehicle Symposium*, 189–191, Berlin, Germany, 2001.
6. Benlamine, R., F. Dubas, C. Espanet, et al., "Design of an axial-flux interior permanent-magnet synchronous motor for automotive application: Performance comparison with electric motors used in EVs and HEVs," *2014 IEEE Vehicle Power and Propulsion Conference (VPPC)*, 1–6, Coimbra, Portugal, 2014.
7. Gao, P., "Design and research of PM in-wheel motor for electric vehicle," Tianjin University, 2015.
8. Yang, S., I. Kakavas, N. J. Baker, et al., "The assembly of a V shape in-wheel motor with reduced mechanical support," *8th IET International Conference on Power Electronics, Machines and Drives (PEMD 2016)*, 1–6, 2016.
9. Wang, X. Y., Z. C. Zhang, P. Gao, et al., "Design and simulation analysis of a novel outer rotor IPM motor used in electric vehicles," *2018 13th World Congress on Intelligent Control and Automation (WCICA)*, 1413–1418, 2018.
10. Solero, L., O. Honorati, F. Caricchi, et al., "Nonconventional three-wheel electric vehicle for urban mobility," *IEEE Transactions on Vehicular Technology*, Vol. 50, No. 4, 1085–1091, 2001.
11. Charles, M., "Nissan's Blade Glider EV aims for efficiency, performance," *Design News*, Vol. 69, No. 1, 24–25, 2014.
12. Xiao, Q., "Electromagnetic design and electromagnetic vibration analysis research of in-wheel motor for electric vehicle," East China Jiaotong University, 2019.
13. Liao, C. J., "Design and electromagnetic thermal analysis of in-wheel motor for electric vehicle," East China Jiaotong University, 2018.
14. He, R. and R. J. Zhang, "Research and development of in-wheel motor drive technology," *Journal of Chongqing University of Technology (Natural Science)*, Vol. 29, No. 7, 10–18, 2015.